Reaction Chemistry & Engineering

High-Throughput Reaction Discovery for Cs-Pb-Br Nanocrystal Synthesis

Journal:	*Reaction Chemistry & Engineering*
Manuscript ID	RE-ART-10-2024-000491.R1
Article Type:	Paper
Date Submitted by the Author:	15-Nov-2024
Complete List of Authors:	Chairil, Ricki; University of Southern California, Chemical Engineering Forsberg, Allison; University of Southern California, Chemistry Brutchey, Richard; University of Southern California, Chemistry Malmstadt, Noah; University of Southern California, Chemical Engineering and Materials Science

SCHOLARONE™
Manuscripts

React. Chem. Eng.

ARTICLE

Cite this: DOI: 00.0000/xxxxxxxxxx

High-Throughput Reaction Discovery for Cs-Pb-Br Nanocrystal Synthesis†

Ricki Chairil[a], Allison P. Forsberg[b], Richard L. Brutchey[b], and Noah Malmstadt*[abc]

Received Date
Accepted Date

DOI: 00.0000/xxxxxxxxxx

High-throughput reaction discovery is necessary to understand complex reaction spaces for inorganic nanocrystal synthesis. Here, we implemented a high-throughput continuous flow millifluidic reactor to perform reaction discovery for Cs-Pb-Br nanocrystal synthesis using a ligand assisted reprecipitation (LARP)-type approach. 3D-printed flow resistors enable the screening of up to 16 different mixing ratios within a single 90 s run, allowing for >270 different precursor concentration ratios to be quickly tested to explore the phase space that results in $CsPbBr_3$, Cs_4PbBr_6, a biphasic mixture, or no product. To construct a full phase map from these high-throughput experiments, a neural network was trained and validated to predict the product composition (∼500,000 points in precursor concentration space). The concentration map predicts product phase as a function of Cs-Pb-Br feed ratio. This approach demonstrates how high-throughput flow chemistry can be used in tandem with machine learning to rapidly explore nanocrystal reaction spaces in flow.

1 Introduction

Nanocrystal synthesis and reaction exploration are increasingly vital to the modern chemical manufacturing landscape.[1] The global market for nanocrystals and related products was estimated at US$7-8 billion in 2020 and is projected to grow 14.1% annually from 2021-2028.[2] This is due to their versatile properties and functions, as well as their utility in many sectors of industry, including medicine, semiconductors, electronics, specialty chemicals, and even consumer goods.[2–4] However, the solution-phase synthesis of nanocrystals can be fickle, and the myriad experimental variables including temperature, time, reagent choice, concentration ratios, and even order of addition can affect nanocrystal nucleation and growth.[5]

Cs-Pb-Br is a ternary materials system that includes the all-inorganic $CsPbBr_3$ lead halide perovskite composition and the perovskite-like Cs_4PbBr_6. Lead halide perovskite nanocrystals represent a class of materials with promising applications in next-generation displays and electronics[6,7], and are typically synthesized using either hot-injection or ligand assisted reprecipitation (LARP) methods.[8,9] The resulting nanocrystal product is highly sensitive to reaction parameters, especially precursor concentration ratios.[10,11,12] Generally, unveiling the dependency of product outcome (e.g., crystal phase and material stoichiometry) on reaction parameters is done *via* batch, one-variable-at-a-time (OVAT) experimentation.[13–16] As the reaction parameter space for nanocrystal production is large and many-dimensional, typical batch OVAT approaches are not only time- and labor-prohibitive, but also incapable of revealing higher-order interactions between the experimental variables and their effects on specific product characteristics or addressing batch-to-batch variability.[4,17–19]

Thus, there is a pressing need for high-throughput (HT) reaction exploration that can rapidly map complex parameter spaces using automated experimental techniques. HT screening systems are capable of processing more than 10^4 samples per day[20], and conducting reactions in continuous flow allows for tight control of reaction heat and mass transfer and fast parametric screening for reaction discovery,[4,18] while also mitigating undesired effects often observed in batch synthesis.[21,22] Here, we use Cs-Pb-Br as a model system to introduce two key innovations in the deployment of high-throughput reaction discovery in continuous flow: parallel variation in reactant stoichiometry to explore compositional space and the development of a phase space map using machine learning.

Continuous flow reactors have been used to discover the reac-

[a] Mork Family Department of Chemical Engineering and Materials Science, University of Southern California, 925 Bloom Walk, Los Angeles, California 90089-1211, United States. E-mail: malmstad@usc.edu
[b] Department of Chemistry, University of Southern California, 840 Downey Way, Los Angeles, California 90089-0744, United States.
[c] Department of Biomedical Engineering, University of Southern California, 3650 McClintock Avenue, Los Angeles, California 90089-1111, United States.
* Corresponding Author.

† Electronic Supplementary Information (ESI) available: [details of any supplementary information available should be included here]. See DOI: 00.0000/00000000.

tion parameters for generating nanocrystals with targeted properties.[23] Off-line analysis can be used to interrogate optically inactive particles[18], but for photoluminescent materials, such as quantum dots and lead halide perovskite nanocrystals, in-line monitoring of optical signatures allows for rapid evaluation of products, facilitating controlled syntheses as well as optimization of reaction parameters.[24,25] Flow platforms for probing reaction conditions for photoluminescent nanocrystal synthesis have primarily focused on optimizing reaction temperature and residence (reaction) time.[26,27] Work on investigating compositional space has relied on varying compositions in an OVAT fashion or utilizing reactors in which each channel is controlled by its own pump system[28,29], increasing system complexity and equipment cost. Here, we explore compositional space by utilizing a new reactor geometry that systematically varies reagent ratios across a network of parallel channels. While such parallel geometries have been utilized for nanocrystal manufacturing[22,23], their use in HT reaction discovery has been limited.

2 Experimental

2.1 Precursor reagent preparation

Cesium carbonate (Cs_2CO_3, 99.9%), lead (II) oxide (PbO, 99.9%), and oleic acid (90%) were all purchased from Sigma-Aldrich (St. Louis, MO, USA). Tetra-*n*-octylammonium bromide (TOAB, 98%) was purchased from Beantown Chemical (Hudson, NH, USA). Hexane and isopropyl alcohol (IPA) were purchased from VWR Chemicals BDH (Radnor, PA, USA). The reagent synthesis and preparation follow Wang *et al.*[22] closely, except hexane is used as the solvent instead of toluene, because toluene is incompatible with the poly(methyl methacrylate)-based 3D-printing resin. Details of Cs(oleate), $Pb(oleate)_2$, and tetraoctylammonium bromide (TOAB) precursor reagent preparation are given in the Supporting Information.

The precursor solutions were transferred to 250 mL bottles with three-holed GL45 caps. One of the holes was plugged and one held the inlet nitrogen gas line for pressurizing the reagent. PTFE intake tubing (1/16 inch inner diameter) was inserted directly into the reagent through the remaining cap hole. Appropriately-sized PEEK HPLC fittings and ferrules from IDEX Health and Science (Northbrook, IL, USA) were used throughout the reactor to make tubing connections.

Reagent viscosities were obtained using a Cannon-Ubbelohde "semi-micro" manual viscometer (Cannon Instrument Company; State College, PA, USA) at 21°C. Reagent fluid properties are provided in Table 1.

Table 1 Reagent viscosities and densities measured at 21°C.

Reagent	Kinematic viscosity ($mm^2\ s^{-1}$)	Density ($kg\ m^{-3}$)
10 mM Cs^+ precursor	0.71	688
10 mM Pb^{2+} precursor	0.65	691
40 mM Br^- precursor	0.98	613
0.317 M oleic acid in hexane	0.49	669

2.2 Product characterization

2.2.1 Powder X-Ray Diffraction (XRD)

Prior to XRD measurement, samples were washed with hexane and pelleted by centrifuging at 4,000 rpm for 5 min. XRD patterns were acquired on a Rigaku Ultima IV diffractometer operating at 40 mA and 44 kV with a Cu K_α radiation source (λ = 1.5406 $\AA$). Powder samples were dropcast on a zero-diffraction silicon substrate.

2.2.2 Transmission Electron Microscopy (TEM)

TEM images were acquired on a Thermo Fisher FEI TALOS F200X microscope operating at 200 kV with a single tilt holder. Each sample was prepared for microscopy by drop casting a sonicated suspension of nanocrystals onto a 400 mesh lacy carbon coated copper grid (Ted Pella, Inc.; Redding, CA, USA) and dried overnight under vacuum at room temperature.

2.2.3 Ultraviolet-Visible Spectroscopy (UV-Vis) and Photoluminescence Spectroscopy (PL)

While most UV-Vis and PL spectra were obtained using the in-line, stage-mounted optical detection unit described in the Supporting Information, additional confirmatory and validation UV-Vis/PL spectroscopy was also performed using a BioTek Synergy H1 multimode microplate spectrophotometer. Typical sample volume, where this system was used, was 100 μL in a 96-well microplate format, corresponding to a pathlength of approximately 2.8 mm.

2.3 Process flow and 3D-printed resistor design

Figure 1 is a schematic diagram of the HT parallel flow reactor we developed to explore the role that reactant stoichiometry plays in the Cs-Pb-Br system. It shows the flow pathway for a single precursor stream. In practice, three precursor streams - one for each element in the product - were combined at the end point of this schematic. These precursors were Cs(oleate), $Pb(oleate)_2$, and tetraoctylammonium bromide (TOAB), which were all dissolved in hexanes and reacted at room temperature.[8] Figure 1 provides the key design methodology used to control stoichiometry across 16 parallel channels of the reactor: the molar ratio of the three precursors in each reaction channel is set by the relative flow rates, which in turn are controlled by the hydrodynamic resistance of each parallel branch. In the low-Reynolds-number (*Re*) regime in which this reactor operates ($Re < 1300$, entrance lengths > 5.75% of the product of *Re* and channel diameter indicating fully developed flow)[30], flow rate is simply the ratio of pressure to hydrodynamic resistance, so a single pressure source at the head of each precursor stream can be used to generate 16 different mixing ratios. The result can be seen at the bottom of Figure 1 as the different mixing ratios generate visually distinguishable Cs-Pb-Br products.

Control of hydrodynamic resistance was accomplished by integrating a set of 3D-printed fluidic resistors (with resistance $R_{res,j}$ in Figure 1; photograph of installed resistors in Figure 2a) in the flow path of one of the precursors (TOAB in practice, although the same control could be achieved with resistors in any of the

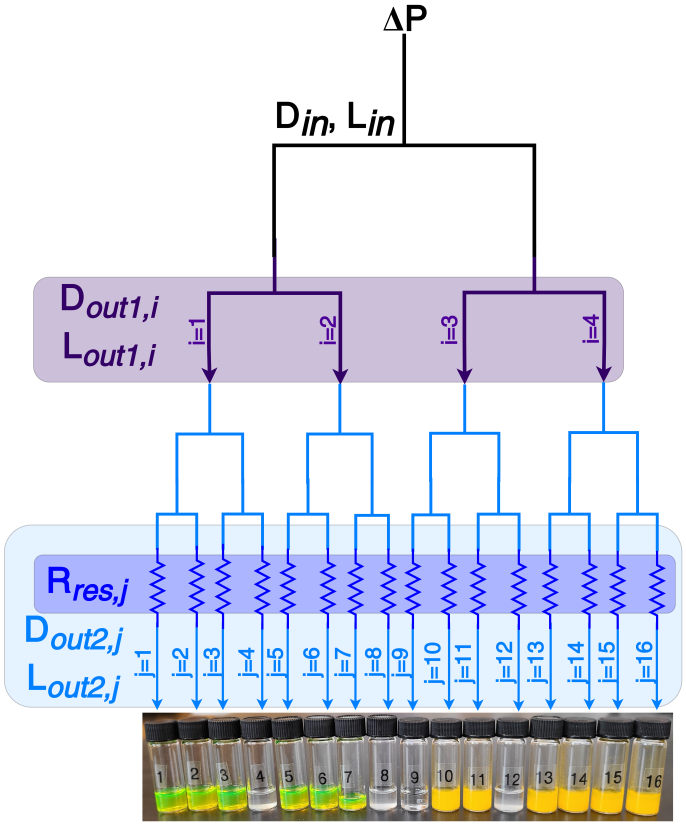

Fig. 1 Schematic of the TOAB (bromide, Br^-) stream, with operational and design elements of the flow reactor. Here, ΔP is the inlet pressure, *D* is diameter and *L* is length. The subscript *in* corresponds to the inlet tubing, subscripts *out1,i* correspond to the i = 1-4 lengths of tubing leaving the first flow manifold, and subscripts *out2,j* correspond to the j = 1-16 lengths of tubing leaving the system. The flow distribution is controlled by the resistances of the 16 3D-printed resistors, $R_{res,j}$. The reactor setup is identical for the Cs(oleate) and Pb(oleate)$_2$ streams, except that no resistors are in place. At bottom: a photograph of the Cs-Pb-Br nanocrystals produced in a representative run on the 16-channel reactor, formed from the various different concentration ratios of Cs-Pb-Br. In channels 1-3 and 5-7: phase-pure $CsPbBr_3$ nanocrystals were obtained; in channels 4, 8, and 12: phase-pure Cs_4PbBr_6 nanocrystals were obtained; in channels 10, 11, 13-16: biphasic mixtures of $CsPbBr_3$ and Cs_4PbBr_6 were obtained, and in channel 9: no reaction.

three precursor flow paths). The design methodology for using 3D-printed resistors to control flow rate is an elaboration of the work of Bhargava *et al.*[31] The hydrodynamic resistance of each resistor is controlled by selecting an internal channel length (typically 100-600 mm) and width/diameter (typically 500-800 μm). The resistors were designed by treating their internal flow as laminar and applying the Hagen-Poiseulle equation for the appropriate channel cross-sectional geometry. Long channel lengths in a small resistor footprint are accomplished by adding 90° bends, making the channels serpentine. Using 3D-printed resistors for flow control affords complete freedom of internal design diameter and length, as opposed to using an off-the-shelf alternative like small-diameter tubing, which is limited to only industry-standard internal diameters and circular cross-sections.

Once the flow rate of TOAB needed to target a certain Cs-Pb-Br mole ratio is known for a given reactor channel j, solving Equation S6 (Supporting Information) for the element resistance $R_{res,j}$ gives the required design resistance. Initial resistors were designed to bracket the TOAB flow rates required to achieve exactly stoichiometric molar ratios of Cs-Pb-Br (hereafter shorthand for [Cs(oleate)]-[Pb(oleate)$_2$]-[TOAB]) required to produce the two stable product species (i.e., x_{Cs}:x_{Pb}:x_{Br} = 0.20:0.20:0.60 for $CsPbBr_3$ and x_{Cs}:x_{Pb}:x_{Br} = 0.36:0.09:0.55 for Cs_4PbBr_6) in a single run. Over the course of the experiments, additional resistors were designed to explore Cs-Pb-Br concentration ratios further away from the two main stoichiometric ratios. Details on resistor design and flow control are presented in the Supporting Information.

2.4 Reactor operation

The three precursor solutions were driven by pressurizing feed reservoirs with nitrogen at a controlled pressure. We used a multichannel flow controller to select the pressure on each reservoir to achieve mixing ratios as described above. Each stream was further split using a series of manifolds into 16 parallel streams. Following splitting into 16 channels, Cs(oleate) and Pb(oleate)$_2$ solution streams were merged. This merged Cs-Pb stream then joined the fluidic resistor-controlled TOAB flow further downstream, producing reactant mixtures with different concentrations of the precursors across each channel. Near the outlet of the reactor, an automated, linear stage-mounted optical detection system connected to an in-line miniaturized spectrophotometer obtains both the absorbance ($\lambda \sim$ 300-800 nm) and fluorescence emission (excitation λ_{ex} = 405 nm) spectra of the 16 product streams within approximately 90 s. This inline monitoring allows distinguishing between luminescent orthorhombic $CsPbBr_3$ nanocrystals and non-luminescent (at 405 nm excitation) trigonal Cs_4PbBr_6 nanocrystals as described below. A full schematic of the reactor is shown in Figure S2 in the Supporting Information.

3 Results & discussion

3.1 Resistor validation

After each resistor was produced, it is necessary to evaluate its actual fluid resistance because of inherent manufacturing variability. This resistor performance was validated using simple flow rate experiments with an inert solvent (hexane and isopropanol, adjusted to the viscosity of the actual reagents) connected to the pressure controller by inlet and outlet tubing of known dimensions. The real fluid resistance determined from the measured flow rate was compared to its intended design resistance. Figures 2b and 2c show results of this resistor validation process. For this data set, 26 different unique resistor designs were tested (with replicates), across 87 different pressure-resistor combinations. Figure 2b shows how measured hydrodynamic resistance varies from as-designed resistance as a function of resistor channel geometry (internal channel length, width, and number of 90°turns) as the driving pressure is changed from 300 to 400 to 800 mbar, for individual resistor designs not yet installed on the 16-channel reactor. Resistance variances over these pressures

span a range between ~2% and ~31% with a slight trend of lower variances for short channels with fewer turns excepting the 31% outlier. Because the %CV is relatively low (i.e. comparable to the %CV in flow variation seen in our previous work with droplet flow parallelization for $CsPbBr_3$ production)[22] regardless of inlet pressure and resistor design, it can be asserted that the linear Ohm's Law-type relationship between pressure, flow rate, and fluidic resistance generally holds for our 3D-printed resistors. As such, we can use such tools as the statistical model developed in the Supporting Information section 2.3, in combination with Equation S6 to link resistor design to a desired flow rate.

Figure 2c demonstrates the ability of the resistor network to control mole fraction of TOAB in the reaction mixture after the resistors are installed. Resistors were mounted on the TOAB stream of the full 16-channel system and the volumetric flow rate of the combined and individual streams leaving each channel of the reactor were measured. The TOAB mole fraction was determined from the increase in flow rate relative to a flow without the TOAB stream. Figure 2c plots these measured mole fractions (x_{Br}) against mole fractions calculated based on the as-designed (i.e., theoretical) hydrodynamic resistances. The data shown here are for a driving pressure of 300 mbar for all reagents; however, flow rates and concentration ratios for each precursor stream were verified for all pressures used in these experiments (50-800 mbar). The dotted 45° line corresponds to perfect alignment between predicted TOAB mole fractions x_{Br} and actual observed x_{Br}; as shown in Figure 2c, the resistors tested resulted in observed Br mole ratios generally very close to their intended design, with the maximum discrepancy being less than 20%. The Supporting Information (sections S3.1-S3.3) gives full details on methodologies used to design/predict hydrodynamic resistance and mole fraction.

3.2 In-line absorbance and photoluminescence

The absorbance and fluorescence emission spectra of a representative run across a range of resistor-controlled concentration ratios are shown in Figure 3. Product identities could be determined from these spectroscopic data. The $CsPbBr_3$ nanocrystals have an excitonic absorption edge at around 400 - 500 nm, with pronounced green photoluminescence (PL) at 500-520 nm from 405 nm excitation.[22,32] The Cs_4PbBr_6 phase has a signature absorbance peak at ~318-325 nm[32] while having no PL from 405 nm excitation in its pure form.[33] These characteristics allow the product spectra to easily be categorized. The presence of both an absorbance edge around 450 nm and a peak around 325 nm, as observed in channels 14 and 15 in Figure 3, indicates a biphasic mixture of both $CsPbBr_3$ and Cs_4PbBr_6.[32] The presence of the metastable $CsPb_2Br_5$[34] phase, which can also have an absorbance maximum at 325 nm[32] but no excitonic edge after 400 nm, was ruled out *via* X-ray diffraction (XRD) analysis (see Supporting Information). Importantly, PL full-width at half-maxima (FWHM) for all emission spectra containing either $CsPbBr_3$ alone or in coexistence with Cs_4PbBr_6 ranged from 26-29 nm, consistent with the threshold for good-quality nanocrystals as defined in our previous work (*i.e.* FWHM < 35 nm).[22]

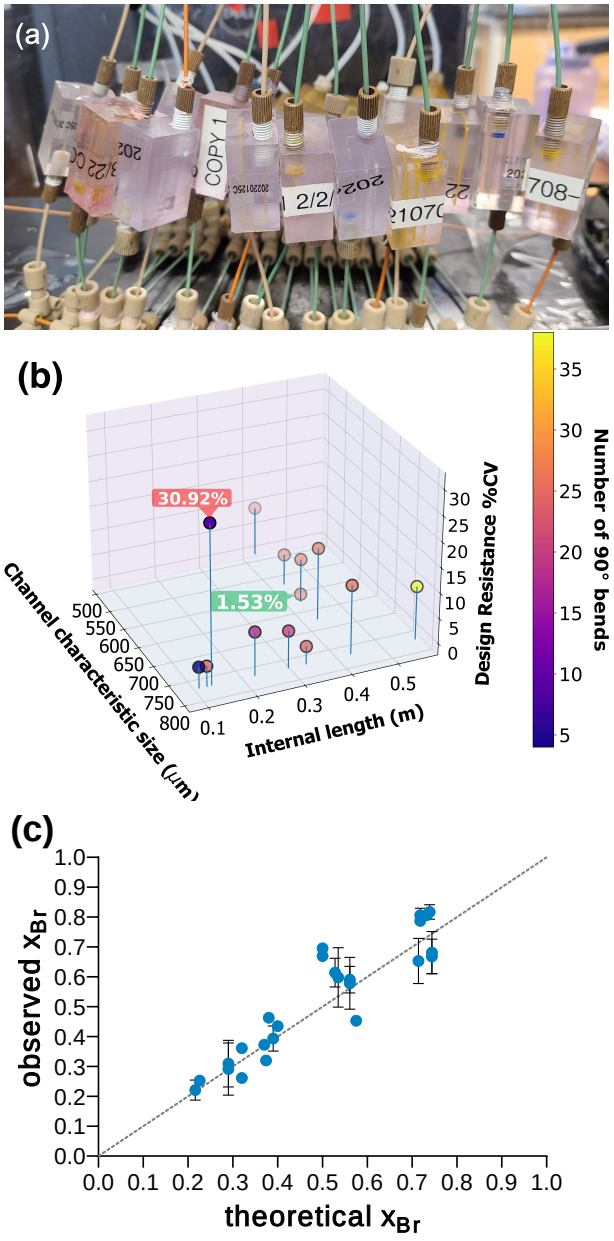

Fig. 2 (a) Photograph of installed 3D-printed resistors in TOAB stream, with connecting tubing; (b) Coefficient of variation (%CV) across three driving pressures for selected 3D-printed resistors as a function of their channel characteristic size, internal length, and number of right-angle bends. Each point represents a unique design, and resistor resistance %CV is from experiments with inlet pressures 300, 400, and 800 mbar. Maximal (red callout = 30.92%) and minimal (green callout = 1.53%) %CVs about these three pressures are shown; (c) x_{Br}, TOAB mole ratios with resistors installed vs. Hagen-Poiseulle prediction. Error bars show one standard deviation above and below (where not shown, the bars are smaller than the data point markers).

3.3 Building machine learning (ML) models to predict HT reaction outcomes

To map the compositional space, we defined Cs:Pb:Br mole ratios of 1:1:3 (orthorhombic) and 4:1:6 (trigonal) as nominal "stoichiometric centers", providing initial guides for the reactant concentration ratios that should yield each product. An ultimate

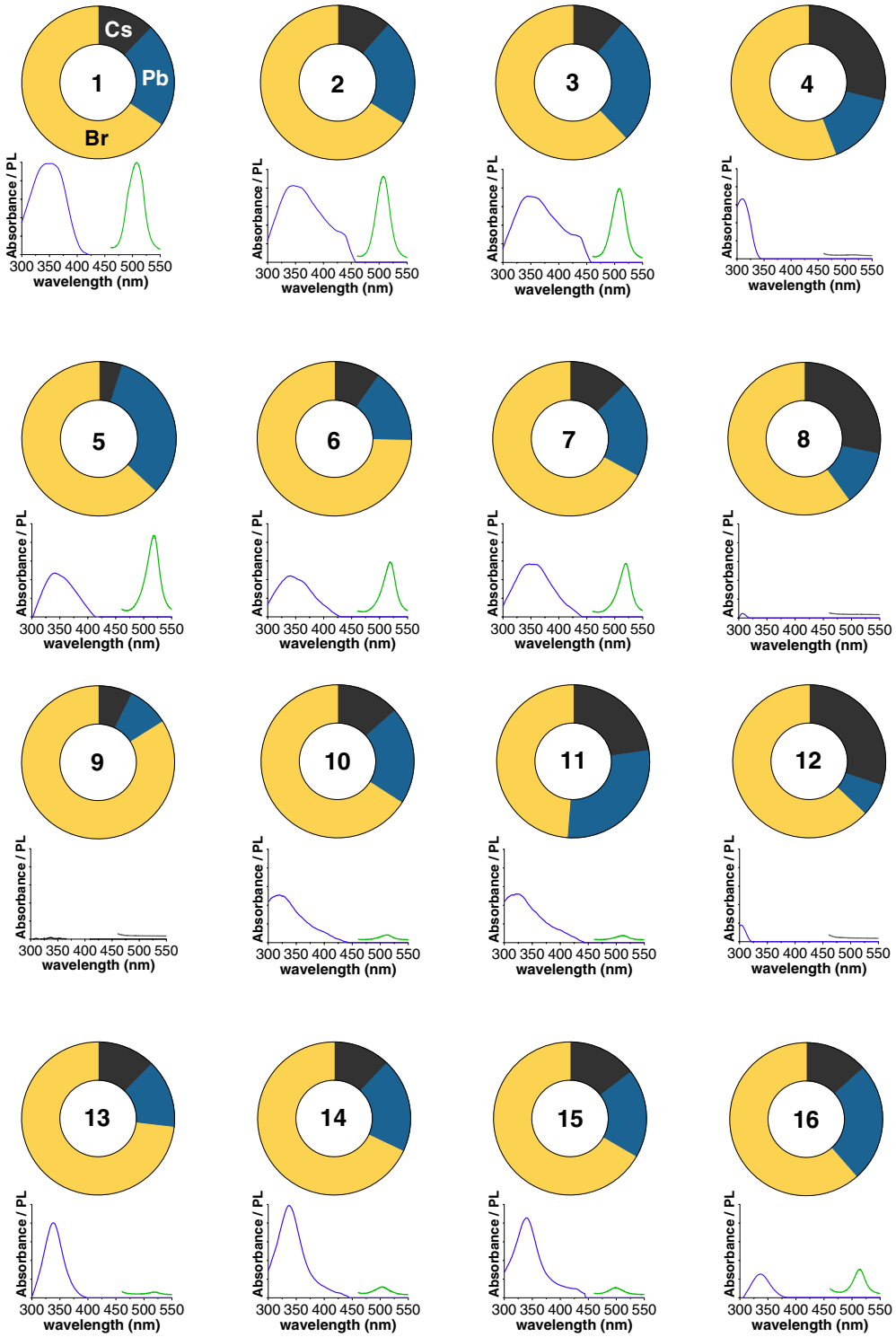

Fig. 3 Representative absorbance (violet curves), PL (green curves for samples containing $CsPbBr_3$, gray for pure Cs_4PbBr_6 or no reaction) spectra with the corresponding mole ratios (donut plots) achieved with 16-channel reactor outfitted with various 3D-printed resistors along the TOAB stream. Channel numbers are indicated in the centers of the donut plots.

objective of this work is to define the boundaries of the ternary concentration space and determine how "far away" from a given stoichiometric center a feed stoichiometry can be while still producing a given phase. To identify the points in reactant composition space that map to each nanocrystal phase product, the HT reactor was used to obtain spectra for 278 different reactant compositions. Each (absorbance/photoluminescence (PL)) pair of spectra was identified as corresponding to $CsPbBr_3$, Cs_4PbBr_6, a biphasic mixture of both, or no reaction. Machine learning (ML) models were then constructed to predict the most-likely

phases of 500,000 x_{Cs}:x_{Pb}:x_{Br} ratios throughout the entire ternary mixing space. Three ML model candidates–k-nearest neighbors (KNC), support vector (SVC), and multi-layer perceptron (MLP) classifiers–were trained on the ground-truth HT discovery data and 30-fold cross-validated, then deployed across the Cs-Pb-Br domain to construct concentration "maps" leading to the four product possibilities listed above. Figure 4 shows the map generated using the MLP model, which had the highest average internal validation accuracy of ∼60% (see the Supporting Information section 2.4 for details and comparison with other models). We note that an average model accuracy of ∼60% is near the maximum for this dataset, since the addition of additional observed data points beyond ∼200 no longer improves model accuracy, indicating sufficient training. This is consistent with machine learning models deployed in similar studies.[35,36]

This phase map illustrates that a Cs-lean (x_{Cs} < 0.3) reaction mixture mostly leads to phase-pure $CsPbBr_3$ or a biphasic mixture of $CsPbBr_3$ and Cs_4PbBr_6, provided enough Br^- is supplied (x_{Br} > 0.3). Below a Br^- mole fraction of *ca.* 0.30, no nanocrystals formed, regardless of the proportion of Cs(oleate) and Pb(oleate)$_2$. Furthermore, the most-likely product space for phase-pure Cs_4PbBr_6 is significantly smaller than that of $CsPbBr_3$, and is consistent with the Cs-rich, Pb-lean concentration boundaries outlined in previous work.[32] There is also a narrow region between the two stoichiometric centers marked mostly by no reaction, despite this area's closeness to the two main phase spaces. Furthermore, some relatively isolated phase regions were also observed, most notably the thin "island" of biphasic mixtures clustered around x_{Pb} ∼ 0.25 and x_{Br} > 0.40 near the $CsPbBr_3$ stoichiometric center. Overall, Figure 4 emphasizes how predicting nanocrystal reaction outcomes simply based on proximity to known stoichiometries can be inaccurate and counterintuitive, and how more sophisticated approaches to reaction discovery are often necessary to elucidate the feasibility regions of these products.

3.4 External validation of ML models

To externally validate this model consistently with best practices, we experimentally challenged it with points in the composition space that were not included in the original training set.[37] Ground truth data for external experimental validation was generated by randomly selecting several locations within the MLP-predicted phase regimes outside the training data and synthesizing nanocrystals with feed compositions corresponding to these points (i.e. points C-E in Figure 4).[38] A point within one of the three main "regions" corresponding to phase-pure $CsPbBr_3$, Cs_4PbBr_6, or a biphasic mixture of the two were chosen, as well as the ternary mole ratios corresponding to the two stoichiometric centers for $CsPbBr_3$ and Cs_4PbBr_6 (A and B respectively in Figure 4). External validation samples were characterized with UV-vis absorbance and PL spectra collected in-line, as well as off-line powder XRD and transmission electron microscopy (TEM). The resulting characterization data for each of the five samples are given in Figure 5, with TEM size data summarized in Table 2; the MLP ML model was successful in defining the most-likely Cs-Pb-Br flow product phases at the selected locations. These results also hold for batch reactions at the same concentration ratios; see Section 3.2 in the Supporting Information for details and characterization data.

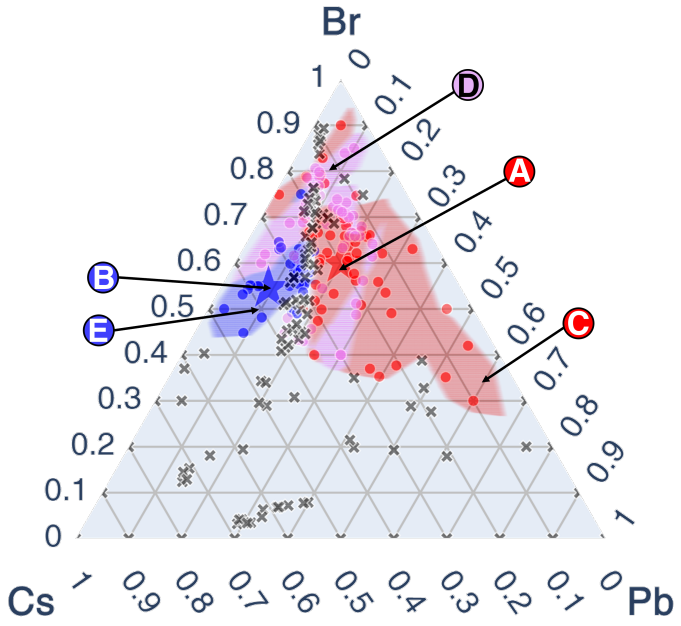

Fig. 4 Cs-Pb-Br ternary phase map (axes = mole fractions) of observed phases as solid circles (● $CsPbBr_3$; ● Cs_4PbBr_6; ● biphasic mixture of $CsPbBr_3$ and Cs_4PbBr_6) or X for no reaction. Theoretical stoichiometric centers are marked with stars (★ $CsPbBr_3$ (Point A), ★ Cs_4PbBr_6 (Point B)). The most-likely product phases between data points are represented as shaded areas (— $CsPbBr_3$; — Cs_4PbBr_6; — biphasic mixture of $CsPbBr_3$ and Cs_4PbBr_6, — no reaction), as predicted by multi-layer perceptron neural network (one hidden layer, 75 neurons, rectified linear activation function, mean model accuracy 60% over 30 folds). Chosen points for external validation are also shown. In terms of Cs-Pb-Br mole fractions, they are (A) (0.20, 0.20, 0.60); (B) (0.36, 0.09, 0.55); (C) (0.05, 0.60, 0.35); (D) (0.12, 0.08, 0.80); (E) (0.40, 0.10, 0.50).

Table 2 Size data for the particles shown in the TEM images in the rightmost column of Figure 5. All sizes were obtained by analyzing *n* particles for each validation point in ImageJ. For conditions A, C, and D, mean sizes given are the shortest dimensions of the particles.

Validation point	*n*	Mean particle size (nm)	Size std. deviation (nm)
A	300	5.5	1.3
B	300	31.7	6.5
C	220	42.9	6.0
D	51	125.5	44.7
E	300	33.6	8.3

Specifically:

- Point A is the exact stoichiometric composition of pure-phase $CsPbBr_3$. Point C was predicted to be pure-phase $CsPbBr_3$ by the MLP model. These samples display excitonic edges around ∼500 nm in their absorbance spectra and have considerable PL emission around 505-520 nm. Furthermore, their XRD traces indicate pure-phase $CsPbBr_3$, and the TEM confirms the cuboidal morphology of $CsPbBr_3$ nanocrystals.

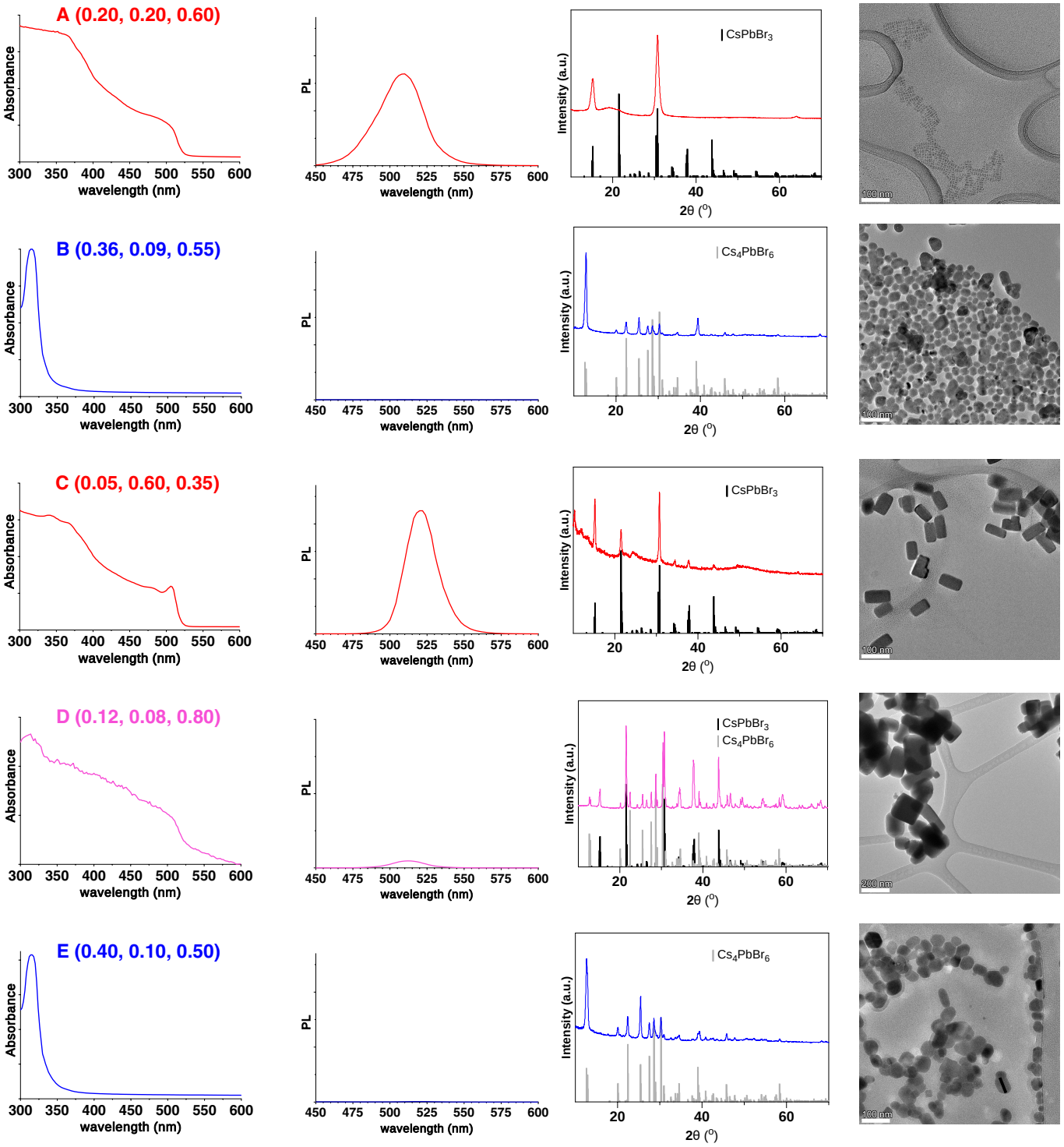

Fig. 5 Characterization data for the external validation points from Figure 4. First column from the left = UV-Vis absorbance spectra; second column = PL from excitation λ_{ex} = 405 nm; third column = experimental XRD traces in red, blue, or pink (reference XRD sticks for $CsPbBr_3$ and Cs_4PbBr_6 are shown in black and gray respectively), fourth column = TEM images; scale bars are 200 nm for sample D and 100 nm for all others.

- Point B is the exact stoichiometric composition of pure-phase Cs_4PbBr_6. Point E was predicted to be pure-phase Cs_4PbBr_6 by the MLP model. These samples display sharp peaks around 320 nm in their absorbance spectra and have no PL emission. Furthermore, their XRD traces indicate pure-phase Cs_4PbBr_6, and the TEM confirms the hexagonal morphology of Cs_4PbBr_6 nanocrystals.[39]

- Point D was predicted to be a biphasic mixture of $CsPbBr_3$ and Cs_4PbBr_6 by the MLP model. This point displays both a

pronounced peak around 320-325 nm and excitonic edge around ∼500 nm in their absorbance spectra, and have slight PL emission around 520 nm from the $CsPbBr_3$ fraction of the mixture. Furthermore, their XRD traces indicate the presence of both $CsPbBr_3$ and Cs_4PbBr_6, and the TEM confirms the coexistence of both $CsPbBr_3$ and Cs_4PbBr_6 nanocrystal structures.

Due to the high-throughput nature of this work, product characterization is chiefly performed *via* rapid in-line spectral analysis; however, if desired, we show here that the product can easily be characterized for size distribution, concentration, imaging *etc.* offline. Furthermore, the two Cs-Pb-Br product phases can easily be distinguished by their absorbance and photoluminescent spectra alone, so in-line spectral monitoring is sufficient for reaction discovery in this case.

While Dahl and coworkers have previously examined the reagent ratios leading to many common Cs-Pb-Br MHP product phases including $CsPbBr_3$, Cs_4PbBr_6, and $CsPb_2Br_5$, their discovery process was performed in-batch using fluid handling robots and focuses on ligand concentration rather than crystal element stoichiometry directly.[32,40] Similarly, Sanchez and coworkers recently described an automated high-throughput reaction screening platform investigating the effect of ligand on the Cs-Pb-Br system, but this platform is again performed only in batch, requires specialized automation equipment, and follows the two-reagent (Cs(oleate) and $PbBr_2$) LARP method at fixed [Cs], which restricts the Pb:Br mole ratio to 1:2.[41] Furthermore, most work including Sanchez *et al.* focuses on optimizing the production of the single $CsPbBr_3$ phase, and evaluates Cs_4PbBr_6 mostly from a kinetic perspective relative to its conversion from $CsPbBr_3$.[32,41] In contrast, the HT system described here does not require costly automation equipment, has a compact footprint (<0.6 m^2), operates in flow, investigates the *a priori* conditions leading to the Cs_4PbBr_6 phase, and employs a straightforward oleylamine-free "three-precursors" method[8,22] (a subset of LARP), which has not yet been evaluated in the context of HT reaction screening. Our synthesis method employs a room-temperature reaction between Cs(oleate), $Pb(oleate)_2$, and tetraoctylammonium bromide (TOAB) precursors in hexanes, similar to a previously reported method by Wei and coworkers.[8] Critically, because we employ three-precursor LARP, the feed stoichiometry is free to take on any combination of Cs-Pb-Br, allowing for exploration of this entire concentration space.

4 Conclusions

The complete compositional phase map (Figure 4) illustrates how HT reaction discovery, coupled with 3D printing-based fluidic design and machine learning models, can be deployed to rapidly explore different product possibilities, even in a complex ternary Cs-Pb-Br reaction system, and even relatively far from nominal phase stoichiometries. Because the discovery process is performed in flow rather than in batch, the results stemming from the three concentration ratios can be monitored *in situ* without the need for additional pumping equipment, while retaining a total theoretical maximum throughput of about 15,000 samples per day. Crucially, this phase map represents the first account of the product phase frontiers for this three-precursor LARP-type reaction.[32,41] This approach further demonstrates the capacity of ML approaches to leverage HT data and produce an externally verifiable prediction of product composition over a full range of reactant stoichiometries.

Author contributions

R. C.: conceptualization, experiments, data analysis and interpretation, and writing
A. P. F.: experiments, data analysis and interpretation, and writing
R. L. B. and N. M.: conceptualization and writing

Conflicts of interest

There are no conflicts to declare.

Acknowledgements

R.C. was supported by a USC Ershaghi Center for Energy Transition fellowship sponsored by Chevron for the HT reactor design and implementation. R.L.B. acknowledges the U.S. Department of Energy, Office of Science, Office of Basic Energy Sciences, under Grant No. DE-FG02-11ER46826 for the materials chemistry and characterization. This work was supported in part by a USC President's Sustainability Initiative Award.

Notes and references

1 M. G. Kanatzidis, *Inorg. Chem.*, 2017, **56**, 3158–3173.
2 A. Barhoum, M. L. García-Betancourt, J. Jeevanandam, E. A. Hussien, S. A. Mekkawy, M. Mostafa, M. M. Omran, M. S. Abdalla and M. Bechelany, *Nanomaterials*, 2022, **12**, 177.
3 T. W. Phillips, I. G. Lignos, R. M. Maceiczyk, A. J. deMello and J. C. deMello, *Lab Chip*, 2014, **14**, 3172–3180.
4 I. Lignos, R. Maceiczyk and A. J. deMello, *Acc. Chem. Res.*, 2017, **50**, 1248–1257.
5 A.-C. Bédard, A. Adamo, K. C. Aroh, M. G. Russell, A. A. Bedermann, J. Torosian, B. Yue, K. F. Jensen and T. F. Jamison, *Science*, 2018, **361**, 1220–1225.
6 P. Cottingham and R. L. Brutchey, *Chem. Commun.*, 2016, **52**, 5246–5249.
7 S. A. Kulkarni, S. G. Mhaisalkar, N. Mathews and P. P. Boix, *Small Methods*, 2019, **3**, 1800231.
8 S. Wei, Y. Yang, X. Kang, L. Wang, L. Huang and D. Pan, *Chem. Commun.*, 2016, **52**, 7265–7268.
9 L. Protesescu, S. Yakunin, M. I. Bodnarchuk, F. Krieg, R. Caputo, C. H. Hendon, R. X. Yang, A. Walsh and M. V. Kovalenko, *Nano Lett.*, 2015, **15**, 3692–3696.
10 T. Udayabhaskararao, L. Houben, H. Cohen, M. Menahem, I. Pinkas, L. Avram, T. Wolf, A. Teitelboim, M. Leskes, O. Yaffe, D. Oron and M. Kazes, *Chem. Mater.*, 2018, **30**, 84–93.
11 A. Pan, B. He, X. Fan, Z. Liu, J. J. Urban, A. P. Alivisatos, L. He and Y. Liu, *ACS Nano*, 2016, **10**, 7943–7954.
12 E. J. Braham, J. Cho, K. M. Forlano, D. F. Watson, R. Arròyave and S. Banerjee, *Chem. Mater.*, 2019, **31**, 3281–3292.
13 L. Mora-Tamez, G. Barim, C. Downes, E. M. Williamson, S. E. Habas and R. L. Brutchey, *Chem. Mater.*, 2019, **31**, 1552–1560.
14 B. Cao, L. A. Adutwum, A. O. Oliynyk, E. J. Luber, B. C. Olsen, A. Mar and J. M. Buriak, *ACS Nano*, 2018, **12**, 7434–7444.
15 E. M. Williamson, Z. Sun, L. Mora-Tamez and R. L. Brutchey, *Chem. Mater.*, 2022, **34**, 9823–9835.
16 E. M. Williamson and R. L. Brutchey, *Inorg. Chem.*, 2023, **62**, 16251–16262.
17 S. Mülhopt, S. Diabaté, M. Dilger, C. Adelhelm, C. Anderlohr, T. Bergfeldt, J. Gómez de la Torre, Y. Jiang, E. Valsami-Jones, D. Langevin, I. Lynch, E. Mahon, I. Nelissen, J. Piella, V. Puntes, S. Ray, R. Schneider, T. Wilkins, C. Weiss and H.-R. Paur, *Nanomaterials*, 2018, **8**, 311.
18 V. Sebastián and K. F. Jensen, *Nanoscale*, 2016, **8**, 15288–15295.
19 E. J. Braham, R. D. Davidson, M. Al-Hashimi, R. Arróyave and S. Banerjee, *Dalton Trans.*, 2020, **49**, 11480–11488.
20 X. Niu, F. Gielen, J. B. Edel and A. J. deMello, *Nat. Chem.*, 2011, **3**, 437—442.

21 D. Perera, J. W. Tucker, S. Brahmbhatt, C. J. Helal, A. Chong, W. Farrell, P. Richardson and N. W. Sach, *Science*, 2018, **359**, 429–434.

22 L. Wang, L. R. Karadaghi, R. L. Brutchey and N. Malmstadt, *Chem. Commun.*, 2020, **56**, 3745–3748.

23 A. M. Nightingale, J. H. Bannock, S. H. Krishnadasan, F. T. F. O'Mahony, S. A. Haque, J. Sloan, C. Drury, R. McIntyre and J. C. deMello, *J. Mater. Chem. A*, 2013, **1**, 4067–4076.

24 S. Krishnadasan, J. Tovilla, R. Vilar, A. J. deMello and J. C. deMello, *J. Mater. Chem.*, 2004, **14**, 2655–2660.

25 J. Nette, P. D. Howes and A. J. deMello, *Adv. Mater. Technol.*, 2020, **5**, 2000060.

26 I. Lignos, V. Morad, Y. Shynkarenko, C. Bernasconi, R. M. Maceiczyk, L. Protesescu, F. Bertolotti, S. Kumar, S. T. Ochsenbein, N. Masciocchi, A. Guagliardi, C.-J. Shih, M. I. Bodnarchuk, A. J. deMello and M. V. Kovalenko, *ACS Nano*, 2018, **12**, 5504–5517.

27 K. Abdel-Latif, F. Bateni, S. Crouse and M. Abolhasani, *Matter*, 2020, **3**, 1053–1086.

28 A. Toyota, H. Nakamura, H. Ozono, K. Yamashita, M. Uehara and H. Maeda, *J. Phys. Chem. C*, 2010, **114**, 7527–7534.

29 R. M. Maceiczyk, K. Dümbgen, I. Lignos, L. Protesescu, M. V. Kovalenko and A. J. deMello, *Chem. Mater.*, 2017, **29**, 8433–8439.

30 T. L. Bergman and F. P. Incropera, *Fundamentals of heat and mass transfer*, Wiley, Hoboken, NJ, 7th edn, 2011.

31 K. C. Bhargava, B. Thompson, D. Iqbal and N. Malmstadt, *Sci. Rep.*, 2015, **5**, 15609.

32 J. C. Dahl, X. Wang, X. Huang, E. M. Chan and A. P. Alivisatos, *J. Am. Chem. Soc.*, 2020, **142**, 11915–11926.

33 Z. Qin, S. Dai, V. G. Hadjiev, C. Wang, L. Xie, Y. Ni, C. Wu, G. Yang, S. Chen, L. Deng, Q. Yu, G. Feng, Z. M. Wang and J. Bao, *Chem. Mater.*, 2019, **31**, 9098–9104.

34 Y. Yin, Y. Liu, G. Cao, Z. Lv, H. Zong, Y. Cheng, Q. Dong, C. Liu, M. Li and B. Zhang, *J. Alloys Compd.*, 2023, **947**, 169439.

35 C. W. Coley, R. Barzilay, T. S. Jaakkola, W. H. Green and K. F. Jensen, *ACS Cent. Sci.*, 2017, **3**, 434–443.

36 G. Vishwakarma, A. Sonpal and J. Hachmann, *Trends Chem.*, 2021, **3**, 146–156.

37 F. Cabitza, A. Campagner, F. Soares, L. García de Guadiana-Romualdo, F. Challa, A. Sulejmani, M. Seghezzi and A. Carobene, *Comput. Methods Programs Biomed.*, 2021, **208**, 106288.

38 L. R. Karadaghi, E. M. Williamson, A. T. To, A. P. Forsberg, K. D. Crans, C. L. Perkins, S. C. Hayden, N. J. LiBretto, F. G. Baddour, D. A. Ruddy, N. Malmstadt, S. E. Habas and R. L. Brutchey, *J. Am. Chem. Soc.*, 2024, **146**, 14246–14259.

39 J. Zhang, A. Wang, L. Kong, L. Zhang and Z. Deng, *J. Alloys Compd.*, 2019, **797**, 1151–1156.

40 M. Imran, V. Caligiuri, M. Wang, L. Goldoni, M. Prato, R. Krahne, L. De Trizio and L. Manna, *J. Am. Chem. Soc.*, 2018, **140**, 2656–2664.

41 S. L. Sanchez, Y. Tang, B. Hu, J. Yang and M. Ahmadi, *Matter*, 2023, **6**, 2900–2918.

DATA AVAILABILITY STATEMENTS

The data supporting this article have been included as part of the included Supplementary Information.

The code for machine learning models developed in this work is available on Github (https://github.com/rchairil/

HTS-16-Ch-Reactor) and are named ternary XXX.py where XXX is the ML method used (KNC, SVC, or MLP).

The code for the in-line spectral acquisition and control systems can be found on Github: https://github.com/rchairil/HTS-16-Ch-Reactor.